

Estimates of performance model factors for passive microseismic SADAR phased arrays at the Newell County Facility

Paul A. Nyffenegger, Elige B. Grant, Jian Zhang, Jason Jennings, Derek Quigley, Kevin D. Hutchenson, Mark A. Tinker, All at Quantum Technology Sciences, Inc.

*Marie Macquet, Carbon Management Canada (CMC)
and Don C. Lawton, University of Calgary, and Carbon Management Canada (CMC).*

Summary

Considering the geographic extent for the large CO₂ geologic sequestration projects required to meet emissions goals, the required measurement, monitoring, and verification (MMV) technology and operations will need to be scalable and cost effective over a duration that extends beyond closure of the reservoir. Networks of passive SADAR phased arrays for microseismic monitoring offer superior data acquisition capabilities using a reduced footprint compared to surface deployed arrays, and phased array signal processing methods produce superior results for detecting and locating microseismic events. A sparse network of four SADAR arrays was installed at the Containment and Monitoring Institute developed and operated Newell County Facility in fall of 2021. After summarizing the development of arrays in global and exploration geophysics, we discuss the array design requirements for being able to fully use phased arrays. The mathematical basis for understanding and evaluating system performance based on the sonar equation is developed. We present observations of noise levels in the frequency domain, and those observations allow several of the factors in the performance model to be estimated, focusing on the observed noise level and the noise suppression useful in determining the array gain. A selection of high-quality events drawn from the SADAR bulletin is used to construct a plot of the measured received-signal-power versus event source-to-receiver range as a function of estimated event magnitude (*i.e.*, source level), in comparison to the measured noise levels also plotted on the graph, showing the basic single channel level and the level after basic processing. From these performance estimates and the results from the bulletin, it is possible to estimate the completeness magnitude of the bulletin at $M_w = -2.5$.

Introduction

Multiple reports have documented the need for capture and storage of CO₂ amounts on the order of tens of gigatons per annum to meet the requirements for worldwide net-emission reductions (IEA, 2020). Geologic carbon sequestration is becoming a required technology for the permanent reductions of carbon dioxide emissions (IPCC, 2021; English and English, 2022). The Global CCS Institute reports for 2021 and 2022 provide summaries and development projections of increasing number of projects opening in the near future; projects in early development number in the 10s. The international Energy Agency states that CCS needs to reach 5.5. GT of CO₂ capture and sequestered per year worldwide to meet the net-zero emission by the 2050 target (IEA, 2020, 2021).

Economical and effective measurement, monitoring, and verification (MMV) technologies help manage the risks associated with underground carbon sequestration, ensure ongoing operations, and verify reservoir integrity beyond the reservoir closure. Lawton *et al.*, (2022) recognize that any CCS reservoir containing volumes upwards of 100 Mt will require substantial MMV efforts much in excess of current pilot studies (Figure 1). Furthermore, injecting CO₂ is more complicated than just reversing of hydrocarbon production; the plume may evolve in ways that models do not predict (Ringrose *et al.*, 2022; Rassenfoss, 2023), and real-time and persistent monitoring is required for detecting transient changes and informing operations.

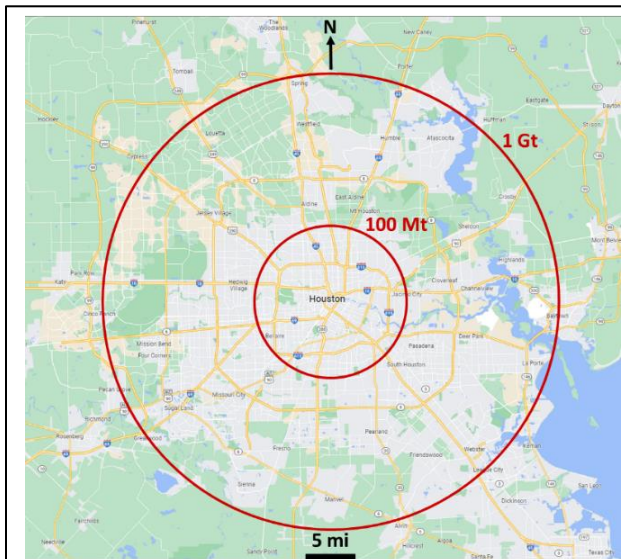


Figure 1: Gigaton CO₂ sequestration plume extent superimposed on Houston street map, after Lawton *et al.*, 2022 (presentation). CO₂ plume extent estimated for a sandstone reservoir formation of 50m thickness assuming 10% porosity, a temperature in the formation of 75C, injection pressure of 25 MPa, CO₂ density of 710 kg/m³, and a storage efficiency factor of 7%.

Active and passive seismic methods continue to be tested as fundamental technologies for remote sensing and monitoring of carbon sequestration reservoirs. The economic and logistical realities of required on-going reservoir monitoring warrant permanently installed robust systems with the minimum number of channels, reduced infrastructure requirements, and minimal surface expression (e.g., Eaton, 2018). Such systems are required to be cost effective, reliable, and maintainable for lifetimes extending well past closure of injection. Extensive networks of surface-emplaced seismic geophones are the most common active and passive monitoring deployments for detecting changes in reservoirs associated with engineering activities. Dense deployments of these geophones have been reported as the most effective configuration for 4-D monitoring using active surveys or used in a passive mode to monitor hydro-fracking operations. However, survey deployments are usually temporary. Only passive seismic monitoring provides a continuous and persistent capability for the sensing and characterization of microearthquakes associated with CO₂ injection, operations, or reservoir failure.

A common approach for detection and location of microseismic events is to use a large network of surface sensors covering the reservoir geographic extent. Noise levels have been recognized as a primary obstacle and overcoming noise levels using surface arrays demands dense sensor deployments and large channel counts in order to produce a bulletin with magnitudes of completeness below Mw 0 and acceptable horizontal and depth location uncertainties. CCS fields are commercial operations with daily industrial activities resulting in a variety of seismic energy sources distributed in location that create a variety of non-stationary noise signals that tend to be coherent; these coherent noise signals clutter the acquired time series. Surface sensor networks mitigate this noise with sheer numbers, fielding large and dense networks that allow using spatial filtering techniques. However, for reservoirs at a gigatonne scale shown in Figure 1, the required

network spatial footprint and number of channels would be incredible in order to reliably detect and locate even relatively large Mw 0 events.

The standard alternative to large surface deployments involves vertical line arrays in boreholes close to the injection well and away from surface noise, allowing the detection of more events at lower magnitudes. Using borehole arrays for detection and location of events to a low magnitude of completeness will require instrumenting many boreholes engineered throughout the monitored volume to reservoir depths of ~2 km. The borehole network will also need to monitor the geologic volume above the active reservoir and discriminate between surface activities and real seismic events, requiring additional sensors deployed towards the surface. Reducing noise via deep borehole emplacements will then come at increased cost and complexity compared to surface networks. Nevertheless, for reservoirs at a gigatonne scale as shown in Figure 1, providing the spatial density required for adequate monitoring of the whole reservoir using deep borehole arrays, as well as sustaining the network, will be complicated and expensive.

Networks of SADAR compact volumetric phased arrays are becoming a proven and economical passive monitoring solution offering technical and economic advantages over surface deployments and deep borehole arrays (Zhang *et al.*, 2023; Zhang *et al.*, 2022; Nyffenegger *et al.*, 2022). Quantum Technology Sciences (Quantum) has installed four SADAR arrays configured as a sparse network at Carbon Management Canada’s (CMC) Newell County facility (NCF) in Alberta, demonstrating an effective monitoring capability (Figure 2). Quantum’s SADAR® system uses a scalable and configurable network of passive SADAR arrays permanently deployed in the shallow subsurface for automatically detecting and locating microseismic events at depth. SADAR arrays can be tuned to meet the design frequencies and wavelengths specific to the site, optimize the signal-to-noise ratio (SNR) of the received signal, determine an unambiguous angle-of-arrival, and determine the phase velocity of the arriving signal. In comparison with surface and near surface dense seismic deployments, SADAR arrays offer a reduced surface footprint and enhanced signal detection and characterization capabilities. In comparison with borehole arrays,

permanent SADAR arrays have a reduced cost for emplacement and more easily accessible and serviced components while still avoiding the majority of the surface noise within the band of interest, and the phased array processing provides superior data quality, unambiguous estimates of direction of arrival, and true phase velocity estimates. In terms of the overall network, the SADAR system architecture is designed for permanent and persistent real-time data acquisition and processing for microseismic monitoring applications, and the SADAR network architecture has the ability to grow incrementally as the state and understanding of the CO₂ plume changes or as the progression of microseismic events dictates

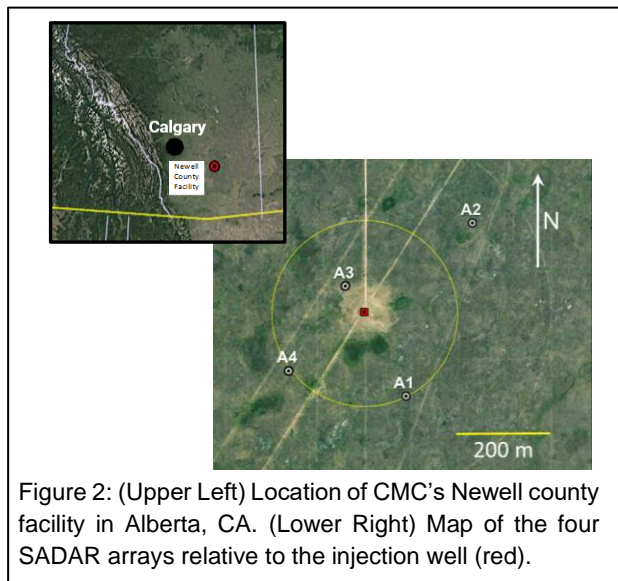


Figure 2: (Upper Left) Location of CMC’s Newell county facility in Alberta, CA. (Lower Right) Map of the four SADAR arrays relative to the injection well (red).

so that the monitoring zone remains within the network.

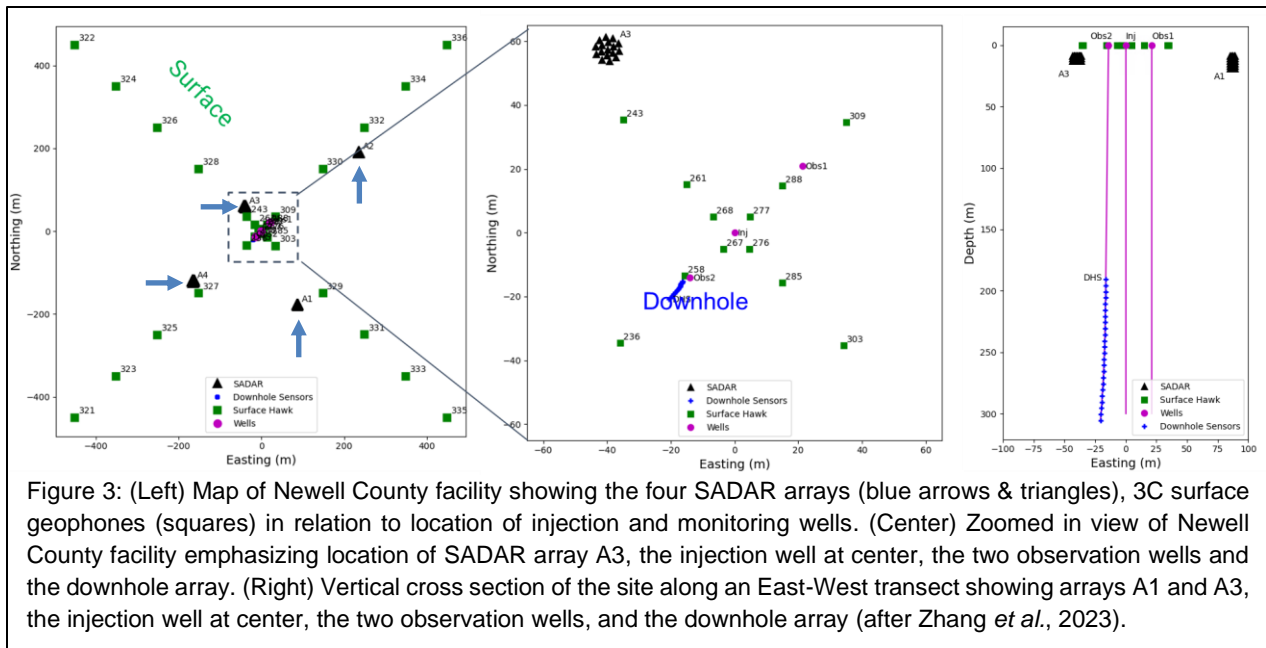
The bulk of this work contains information about the fielded SADAR arrays and a discussion on phased array design, followed by mathematical analysis of the physical and processing system factors affecting performance, and observations of signals and noise for some of the seismic instrumentation at the NCF. An assessment of the noise observations and how those fits into the performance framework follows, as well as an assessment of the noise suppression of the arrays and the performance of received signal versus range for the network of arrays.

Field Setting

The Containment and Monitoring Institute, a division of Carbon Management Canada (CMC) Research Institutes, in collaboration with the University of Calgary, developed and operates the 200-hectare Newell County Facility (Figure 2) located in southern Alberta, Canada (Lawton *et al.*, 2019). The Newell County facility is currently simulating an unplanned CO₂ leakage from a deeper/larger scale CO₂ storage project via injection of ~10-30 tonnes/year of CO₂ into the Basal Belly River Sandstone (BBRS) reservoir at ~300m depth (Macquet *et al.*, 2022). The BBRS is a well-studied seven-meter thick shoreface horizon composed of sorted quartz grains with ~11% average porosity and with maximum permeability of ~0.8 mD (Dongas and Lawton, 2015; Osadetz *et al.*, 2015; Vocke *et al.*, 2016; Muravieva *et al.*, 2017; Jafari Raad *et al.*, 2021). The Upper Cretaceous Foremost Formation caprock that forms the reservoir seal is a 152 m thick clayey sandstone with interbedded coal layers.

The objective for the Newell County Facility is to develop and improve CO₂ measurement, monitoring, and verification (MMV) technologies for minimizing risks associated with geologic CO₂ storage (e.g., containment failure). Simultaneous monitoring at the Newell County Facility using multiple networks and sensor types provides a unique opportunity to compare the detection and location performance for a variety of sensor arrangements and/or processing approaches to prioritize those that offer cost-effective and robust verification of CO₂ containment (Lawton *et al.*, 2019; Macquet *et al.*, 2022). For microseismic monitoring specifically, the site features a string of 24 3C geophones within one monitoring well (Figure 3), 7 broadband seismometers emplaced 1m deep, and 28 3C geophones emplaced 1m deep (Figure 3) (Savard *et al.*, 2020).

In November of 2021, Quantum, in cooperation with Newell County facility management, installed a sparse network of four permanent SADAR compact volumetric phased arrays, shown in Figure 2 and Figure 3, designed specifically for passively monitoring microseismic activity associated with the CO₂ injection activities. Detections on four arrays is the minimum number enabling overdetermined event location procedures that yields both the location and the uncertainties in origin time, horizontal location, and depth. Array A3 is the closest to the injection well at 70m to the north-west, arrays A1 and A4 are located 200m south-west and south-east respectively from the injection well, and array A2 is the furthest at 300m to the north-east from the injection well, all with topmost depths at ~9m and vertical extent contained within the Pleistocene-Holocene sediments and glacial till layer. All elements in all arrays are filled by Geospace GS-ONE 10 Hz vertical-only geophones, and all are acquired as separate channels at a 2000 samples per second rate.



These four arrays test three different SADAR array designs based on uniform cylindrical array (UCA) geometries with diameters ranging from 4m to 7.5m (Figures 4 and 5). Array design (1) the “Standard” UCA configured as an octagon with a central axis and six uniformly vertically spaced levels, and used in deployed arrays A1 and A2 (located in Figures 2 and 3). Array design (2), shown in Figure 5, is the “Wide Aperture” layout configured to have a larger radius as nested UCAs with the outermost arranged as a decagon and the inner as a hexagon with three uniformly spaced levels, designed with improved aperture for waves with a more vertical incidence balanced with the need for a broad bandwidth response and to separate clutter arriving with a more horizontal incidence, and used in array A3. Array A4, also shown in Figure 5, uses the design (3) “Hybrid” approach combining features of the “Standard” array and the “Wide Aperture” design, with the outer UCA having three levels, and the inner hexagon UCA having six. In addition, at the A2 array, the Quantum installation included a surface tripartite array of Geospace GCL 3C packages using GS-SMG 10 Hz sensors, combined with a single small aperture array at one of the vertexes of the tripartite array all acquiring at 2000 samples per second, to be used as a receiver group mainly for noise comparison purposes (Figure 4). The GCL cluster design intentionally used spacings where low frequency noise should be correlated as a test of noise independence.

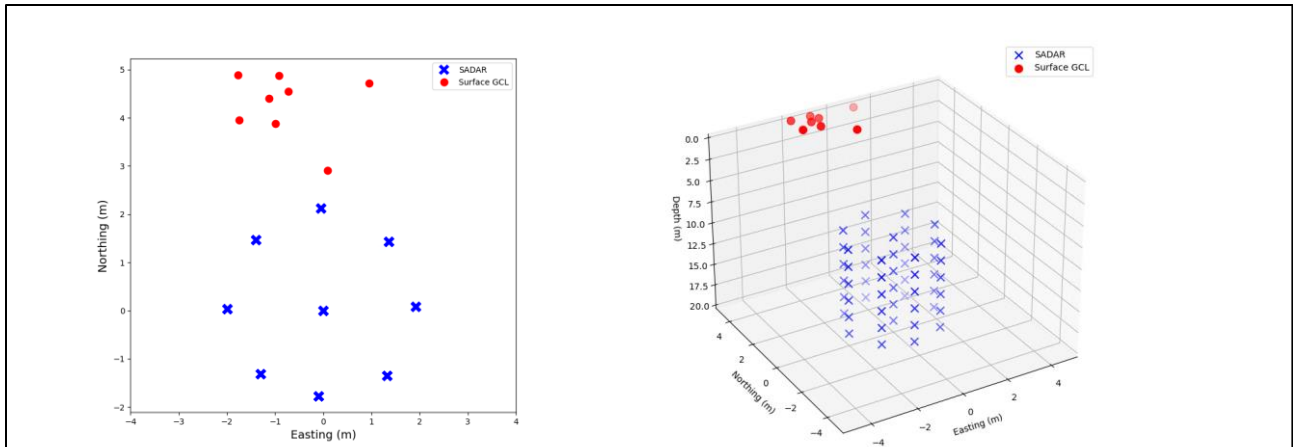


Figure 4: Array design (1) – “Standard” shown at left in map view and right in a three-dimensional view, designed as a uniform cylindrical array with a vertical central axis of configured as an octagon with six levels with uniform spacing of 2m between levels. Design (1) is used for arrays A1 and A2. All array elements are Geospace GS-ONE 10 Hz vertical phones. An additional surface cluster of Geospace GCL units with 10 Hz GS-SMG phones was emplaced above A2 for noise comparisons.

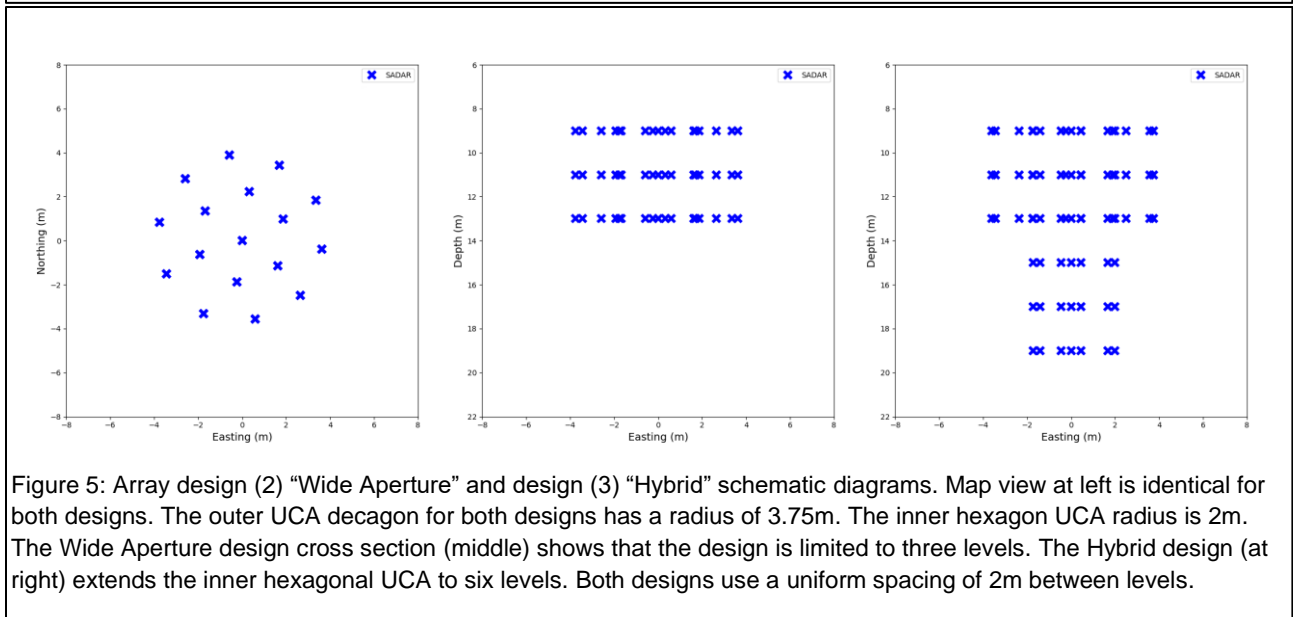


Figure 5: Array design (2) “Wide Aperture” and design (3) “Hybrid” schematic diagrams. Map view at left is identical for both designs. The outer UCA decagon for both designs has a radius of 3.75m. The inner hexagon UCA radius is 2m. The Wide Aperture design cross section (middle) shows that the design is limited to three levels. The Hybrid design (at right) extends the inner hexagonal UCA to six levels. Both designs use a uniform spacing of 2m between levels.

Background

The general technique of arranging Individual sensors into geometric groupings, *i.e.* arrays, has been used in signal acquisition and measurement since around the time of World War-One and is now ubiquitous in virtually every sensing domain that takes advantage of modern digital signal processing. Within this work we use the term *phased array* in the traditional sense described in Van Trees (2002), Frank and Richards (2008), and Ziomek (1995) such that the overall phased array system of sensors and acquisition components enables signal processing methods that take

advantage of the spatial coherence of the signal of interest. The term *coherent processing* here is synonymous with *phased array processing* and reserved exclusively to mean spatially-coherent processing such as beamforming, where signals acquired with a phased array of point sensors are cooperatively manipulated based on the coherence of signals propagating across the array to derive multiple simultaneous directional “beams” specified by the beam main response axis (MRA) pointing outward from a defined reference point. The term *point sensor* is defined such that the dimensions of the sensor are much smaller than the wavelength of the maximum seismic frequency of interest *i.e.* as a sensor that measures the applicable field at a single point rather than as a distributed sensor that integrates signal measurements over a finite aperture. Array elements are the locations of the point sensors, and may be occupied by single sensors, or multiple vector sensors as is the case with triaxial geophone packages.

The signal processing methods for exploiting phased arrays are well-developed across multiple disciplines such as radar (*e.g.*, Skolnik, 2001; Van Trees, 2002), sonar (*e.g.*, Ainslie, 2010; Abraham, 2019), and acoustics (*e.g.*, Mueller, 2002; Michel, 2006;), and for seismology, array processing has a rich history. Both Husebye and Ruud (1989) and Douglas (2013) trace the history of passive seismic phased arrays applied to global nuclear monitoring to the late 1950’s, at about the same time that the US government began project VELA-UNIFORM. Global seismology phased array processing methods and results are now explained in textbooks (*e.g.*, Aki and Richards, 1980; Lay and Wallace, 1995; Ammon *et al.*, 2021), topical monographs and operator manuals (*e.g.*, Havskov and Alguacil, 2006; Havskov and Ottenmoller, 2010; Douglas, 2013; Schweitzer *et al.*, 2012), and subject review papers (*e.g.*, Husebye and Ruud, 1989; Rost and Thomas, 2002).

Global seismic monitoring has focused on detection and characterization of impulsive transient (IT) signals originating with earthquakes and underground nuclear explosions, *i.e.* short duration, broadband signals. Passive undersea monitoring also includes narrow-band signals of extended duration commonly called continuous waveforms (CWs) and frequency modulated waveforms (FMs) generated by watercraft. Engine driven and electromechanical equipment commonly used in construction, industrial activities, and even everyday society generate similar vibrational signals and it is no surprise that seismic sensing systems also acquire these signals. For the frequency band used in seismic exploration, petroleum engineering, and local security applications, such discrete nonstationary sources generating coherent signals are a primary cause of interfering noise generally called *clutter* in sonar and radar systems.

Seismic arrays for global monitoring are traditionally clustered sensors deployed at spacings that enable the analysis of the received signals as a wavefield (Ammon *et al.*, 2021). Arrays having apertures of several kilometers to ~25 km for regional monitoring have been integrated into the global seismic monitoring infrastructure over the last ~50 years. Local area monitoring applies these concepts for industrial and security applications for areas ranging from 10s of meters to 10s of kilometers using local passive seismic arrays with element spacings on the order of meters and apertures on the order of 10 meters or smaller (*e.g.*, Tinker *et al.*, 2021).

Using analog receiver groups for exploration seismology predates WW2. Some early papers on the development and use of these analog arrays in active seismic surveys include Rieber (1936), Klipsch (1936), and Johnson (1939). At this early stage in the development of seismic exploration techniques it was recognized that geometric arrangements of sensors offered a way of reducing

the coherent noise originating at shot points. Both the advantages, the problems, and the physical and mathematical description of using receiver groups of a fixed design have been explored in the nearly 100 years since (e.g., Smith 1956; Denham 1963; Newman and Mahoney, 1973; Cordsen *et al.*, (2000), Baeten *et al.*, (2001), Cortes *et al.* (2015), Dean *et al.*, 2015).

The fixed-design linear analog arrays employed for receiver groups in active surveys provide a single response pattern for emphasizing reflected plane waves such that the angle of incidence on the horizontal array is more vertical. The apparent wavenumber of narrow angle reflections will be low, compared to surface waves propagating from the shot point, so the receiver group functions as an analog low pass wavenumber filter (e.g., Newman and Mahoney, 1973). However, the array response is three dimensional and symmetric about the receiver group axis; any other noise energy arriving at a roughly broadside orientation to the array will also have a low apparent wavenumber and not be filtered.

The move to single-sensor digital sensor data acquisition has influenced survey designs to enable more flexible processing post acquisition including true digital phased array processing (e.g., Roux *et al.*, (2014)). Nevertheless, it is important to understand that both the global monitoring mission and the exploration applications primarily have used two dimensional arrays in linear or planar geometries, with responses best described as a function of apparent velocity, apparent slowness, or apparent wavenumber.

Array Requirements and Array Design Considerations

The beamforming operation in phased array processing shifts the relative phases of the acquired data such that signals recorded by each sensor can be aligned (via time delay/advance) and summed to maximize the power of the received signal propagating across the array in a specific direction and with a specific speed compared to the incoherent noise and coherent signals arriving from other directions and/or at other speeds. This beamforming operation decomposes the wavefield into directional components oriented along the defined beam main response axes (MRAs) such that signals originating from sources that are spatially apart can themselves be separated. Array SNR gain depends on the pairwise cross-correlation coefficients between the elements of the array; arrays of identical designs in differing noise fields will have different array gain (Urlick, 1983). Obviously then the gain of the array degrades as the signal coherence decreases or as noise coherence increases.

For the elements to be processed cooperatively as a phased array, the measured wavefield must be coherent across the array, and it must be equally measured across the array, implying that each element must be coherent in time, frequency and phase, and space with respect to the other elements in the array. Coherence in time dictates that all data acquisition components must be on the same clock or that differences between the clocks be much smaller than the final sample rate, and that no differential time delays are added to the measurements output by the sensors across the array. Coherence in time also requires then that there is little differential wavefield time distortion as the energy propagates from the source to the array; the temporal coherence factor in sonar and radar systems is an important consideration for dynamic media (e.g., Yang, 2006) but not a general concern for seismic applications.

Coherence in frequency and phase requires that the sensors have identical frequency and phase responses over the band of interest such that the sensor does not add any phase factors, shifts, or distortions to the received signal differing from that of any other array element. Likewise for

sensors with a directional response, that the sensitivity patterns are identical from sensor to sensor and are aligned when emplaced. This also requires identical processing of the channels such that operations like channel equalization do not produce differential phase shifts.

Coherence in space dictates that the elements must be located with a precision much greater than a fraction of the shortest wavelength of interest, and that the array aperture be within a “coherence length” of the shortest wavelength of interest to not detrimentally affect gain. A *wavelength-normalized coherence length* is defined as the distance at which the pairwise coherence falls below $1/e$ and estimated using the narrow-band coherence function, broadband correlation function, or coherent SNR gain from either pairwise direct measurements obtain from either a filled aperture or the steered beam response from a sparsely filled aperture (Cary, 1998). Factors affecting the coherence length also effect the beam width and array gain, and include multipath interference, and refractive and scattering effects attributed to inhomogeneities, interfaces, and roughness at interfaces (Cary, 1998). Scattering by inhomogeneities generate travel time fluctuations when considering wavefield arrivals at equidistant point sensors (Shapiro and Schwarz 1995; Shapiro and Schwarz 1996). The overall effect is that array coherence lengths are dependent on the signal propagation distance as well as wavelength.

The overall geometry and inter-element spacing d of the array elements (also known as stations in global seismology) are determined depending upon design frequencies f_d , media velocities c_p and c_s , coherence lengths, and the understanding of the noise field. Equally important considerations include the desired beam width, the directivity index or array gain, and response pattern variability with beam MRA orientation. The design wavelength is then $\lambda_d = c/f_d$ and the ideal element spacings d are derived from the design wavelength as $d = \lambda_d/2$. Because seismic propagation involves multiple types of waves traveling at different phase velocities, an array with a single element spacing d will correspond to more than one design wavelength.

For passive monitoring, a large array aperture is desired to provide a narrow beamwidth and a more precise estimation of the direction of arrival of the signal-of-interest (SOI) with a geometry largely designed to spatially sample the wavefield. However, arrays with aperture larger than the coherence length will not generate a greater gain since adding elements and increasing the aperture adds only noise to the resulting beam (Urlick, 1983). Therefore, the coherence length of the signal of interest is a fundamental limit to spatial coherent signal processing (Cary 1998). For a particular aperture, increasing the number of sensors and reducing sensor spacing with an accompanying increase in the design frequency will increase the gain so long as the noise remains uncorrelated between sensors. Likewise, then, the correlation distance, defined as the separation distance at which the pairwise coherence in the noise drops below a threshold usually set at ~ 0.5 and taken as the minimum spacing needed for a statistical independence of noise in the data, also needs to be considered as a fundamental limit (see for example, summary in Dean *et al.*, 2015). This correlation distance reflects the point at which increasing the number of sensors with a decreasing spacing has a diminishing return on the array gain due to the correlation of the noise.

As is being more commonly considered for surveys in general, the phased array design must also take into account the expected coherent clutter signals propagating throughout the monitored volume (e.g., Strobbia *et al.*, 2022; Krohn *et al.*, 2008). It may be impossible to come to a complete count and review of the number of publications in the last 50 years focusing on the many aspects

of seismic noise and the ensuing discussions covering both monitoring and exploration applications. Nevertheless, a simple, common observation is that for many CO₂ monitoring cases, the coherent noise will be huge and have no stationary spatial preference. To summarize then, a primary design goal for a phased array is to create the largest aperture warranted under the coherence length, using the array element separation that is warranted under the correlation distance required to suppress the noise wavefield and separate signals, for the relevant design frequency and bandwidth.

SADAR Array Design

The SADAR arrays are referred to as “compact volumetric phased arrays” to distinguish the designs from extended linear or planar sensor deployments, or combinations thereof. The arrays are compact both when compared to surface deployment areal coverages and mathematically; the set of array elements at the greatest distances from the array centroid form the vertices of a convex polytope.

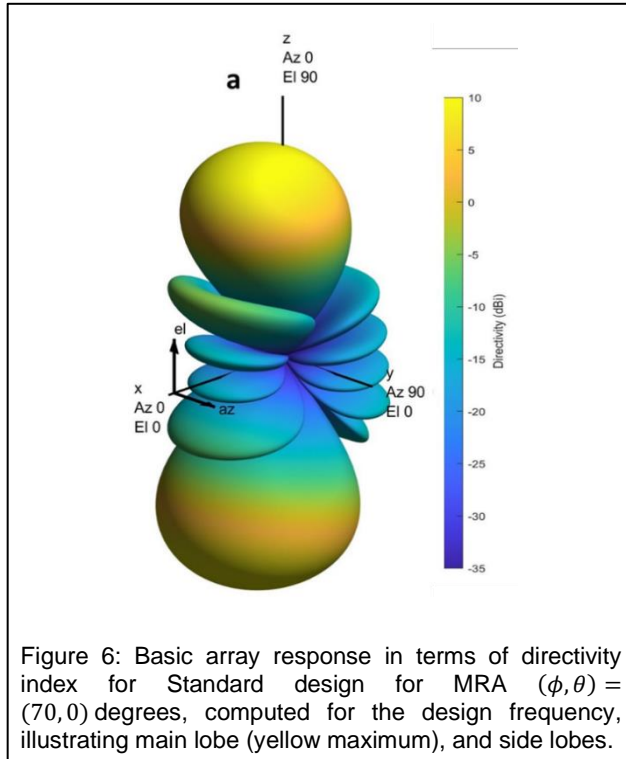
The geometry of a basic compact volumetric phased array is shown in Figure 4 as a uniform cylindrical array with a center column. In phased array design, array response patterns are typically compared for understanding the beam width and side lobe response. The total aperture of the array is set within an expected coherence length for the design frequency and the medium wherein the array is emplaced, and the expected geometry of the wavefronts associated with the signal of interest. The uniform cylindrical array of Figure 4 takes advantage of two primary design frequencies, yielding two fundamental element spacings based on the radius and spacing between levels for P waves (in this example). Nevertheless, the diversity in pairwise element spacing across all 54 elements provides an overall broader band array response pattern.

Array response patterns are commonly shown in two dimensional plots resembling antenna patterns, as a function of frequency, wavelength, or wavenumber, or their apparent counterparts, and angle of arrival of the signal (e.g., Newman and Mahoney, 1973; Havskov and Alguacil, 2006; Schweitzer *et al.*, 2012; Douglas, 2013). Nevertheless, the array response is three dimensional.

The basic array response pattern shown in Figure 6 for the array of Figure 4 appears as a complex solid. The pattern is given for a single frequency, close to the design frequency. Using the compact volumetric phased arrays enables mitigation of coherent signals arriving from arbitrary directions and separation of unrelated simultaneously-arriving-signals that cover the same frequency spectrum but that originate with sources at different locations, none of which is possible with small aperture or element count arrays (e.g., Swanson and Culver, 2017).

However, the spatial filter provided by phased array processing is never perfect resulting in side lobes that may be modified using a variety of approaches, and likewise the width of the main lobe may also be modified. Nevertheless, the derived beam having MRA aligned with the angle of arrival of the signal provides the optimal SNR for estimating the received signal.

Furthermore, sampling the incident wavefield in all three dimensions allows the direct measurement of the phase velocity. Linear arrays produce a directional ambiguity in azimuth and depression angle (dip) about the array axis, as well as limiting velocity resolution to “apparent velocity.” Circular and patch arrays deployed along the surface remove the azimuthal ambiguity but not the ambiguity in depression angle because of reliance on apparent velocity. Furthermore, using any planar array deployed along the surface, as the incident wavefield approaches vertical, any phase velocity resolution is lost.



For SADAR arrays, the number of elements and spacing of boreholes is set to provide a uniform azimuthal response pattern, a desired gain, the estimated statistical independence of the noise in the channel down to $\frac{1}{4}$ of the design wavelength, as well as considerations on the economics of permanent installation in multiple but relatively shallow boreholes. The depth of the top-most sensors is set considering the near-surface noise, near-surface geology and disturbance, and stratigraphic layering over the vertical aperture of the array. The network of arrays is designed based on the estimated performance of the individual arrays, discussed below.

For SADAR arrays, the number of elements and spacing of boreholes is set to provide a uniform azimuthal response pattern, a desired gain, the estimated statistical independence of the noise in the channel down to $\frac{1}{4}$ of the design wavelength, as well as considerations on the economics of permanent installation in multiple but relatively shallow boreholes. The depth of the top-most sensors is set considering the near-surface noise, near-surface geology and disturbance, and stratigraphic layering over the vertical aperture of the array. The network of arrays is designed based on the estimated performance of the individual arrays, discussed below.

System Analysis

This description of the received signal is presented from the perspective of the sensor (or receiver) located at a fixed point (x, y, z) and receiving a field of energies containing a mixture of the signal of interest and competing clutter signals as well as a variety of environmental noise processes. The response of the individual sensors to the total wavefield is the measurement of the received signal, modeled using the standard approach as a linear function of present and past values and independent noise processes but in consideration of the cluttered operating environment:

$$y(t, f) = \sum_k [s_k(x, t, f)] + n_a(\cdot) \quad (1)$$

where $s_k(x, t, f)$ is the received signal from any number k of discrete signal or clutter sources, and $n_a(\cdot)$ is the additive noise encompassing all noise processes in the environment. Depending upon wavelength, $n_a(\cdot)$ may be correlated between elements and may not be azimuthally isotropic or truly random in phase.

An expansion of the model is convenient for categorizing the types of noise and signals:

$$y(t, f) = S(x, t, f) + \sum_k [s_k(x, t, f)] + n_a(t, f) + n_a(f) \quad (2)$$

where $S(x, t, f)$ is the high-interest received signal in the defined analysis frame originating with the source of interest, $s_k(x, t, f)$ represent all the undesired k coherent clutter signals received

simultaneously and from multiple directions, $n_a(t, f)$ is the non-stationary additive noise, and $n_s(f)$ is the stationary additive noise. For the purposes here, stationarity is considered up to order 2 over a time of several analysis frames such that a stable estimate of the probability distribution is possible (Priestley, 1981). *Non-stationary* then can be considered as an “instantaneous” measurement over a single analysis frame and does not have restrictions on its distribution function. If k is a small number and clutter sources are widely spatially separated, it may be possible to reduce the coherent clutter signal term to a simple quantifiable term $n_{ac}(x, t, f)$, but that is not the general case without quantifying these components, and generally will be changing even over the course of a few hours.

Given $y_i(t, f)$ the suite of received signals from the individual array elements i with locations (x, y, z) , let $\Psi()$ represent processing operations acting across all $y_i(t, f)$ for an analysis frame such that a processed continuous series $\alpha(t, f) = \Psi(y_i(t, f))$ may be derived. For example, $\alpha(t, f, \phi, \theta)$ may represent the series from a beam processed to emphasize a MRA along the vector (ϕ, θ) from the array centroid aligned with the direction of arrival of our particular $S(x, t, f)$. The noise in $\alpha(t, f)$ and the coherent clutter signals $s_k(x, t, f)$ not aligned along the beam MRA are suppressed by whatever series of operations comprise $\Psi()$, but the coherent signal $S(x, t, f)$ is largely unmodified.

The primary problem becomes identifying the SOI $S(x, t, f)$ and extracting characteristics and deriving information pertinent to $S(x, t, f)$ from $\alpha(t, f)$, in the presence of competing and interfering unknown signals originating with sources that are not of interest, all embedded within a variety of unknown noise. To parameterize this problem, we follow sonar system analysis as given in Urick (1983), Burdic (1991), Ainslie (2010), and Abraham (2019) among others. The sonar description development is easily recognized as sharing commonality with Boatwright and Choy (1986), Choy *et al.*, (2001), and Boatwright *et al.*, (2002). Following a signal detection paradigm, some measure of the presence of the signal derived from $\alpha(t, f)$ is required to detect the presence of the SOI, and then that measure must surpass a minimum threshold to achieve a required probability-of-detection. For example, a common measure is the short-term average power written $|\alpha(t, f)|$. Casting that measure in terms of SNR power \mathcal{S} (as a function of frequency),

$$E[\mathcal{S}] = \frac{|\alpha(t, f)|}{E[\text{noise}(\alpha(t, f))]} \geq \text{threshold} \quad (3)$$

where $E[\cdot]$ is the expectation operator, it is obvious that the noise power component representing the estimate of the ambient noise present in the derived series $\alpha(t, f)$ must be statically estimated over several analysis frames, and the signal component in the numerator is contaminated by the instantaneous noise. It is common practice to cast the detection equation expression into decibels yielding:

$$10 \log_{10}[E(\mathcal{S})] \geq 10 \log_{10}(\text{threshold}) \text{ dB re: power} \quad (4)$$

or using the common symbol "DT" for the detection threshold in decibels

$$10 \log_{10}[E(\mathcal{S})] \geq \text{DT dB re: power} \quad (5)$$

The signal excess SE can then be defined as the portion of the SNR power that is greater than the detection threshold as a general measurement of the amount of signal we have to work with.

$$SE = 10 \log_{10}[E(S)] - DT \quad . \quad (6)$$

Rewriting the detection equation (5) and breaking the SNR power into individual factors yields:

$$DT \leq (SL - RP) - PL - (NL_f - AG - SP) + PG \quad . \quad (7)$$

where SL is the source level ; RP is the radiation pattern of the source; PL is the propagation loss, a compound term; NL_f is the noise spectrum level, a compound term; AG is the array gain, SP is the sensitivity pattern of the sensor element itself; and PG is gain due to signal processing after the initial beamforming stage, but still considered within $\Psi()$. The radiation pattern factor RP acts as a modifier to the source level SL and is zero for an omni-directional source; herein we will consider SL and RP terms together. The sensitivity pattern factor SP is equal to zero for an omni-directional receiver but needs to be computed for dipole receivers; for the time period, for our purposes here, we will neglect SP . In these types of gross parameterizations, frequency dependence is implicitly considered in each term, and a specified frequency band accompanies whatever numbers are reported.

The expression for signal excess then becomes

$$SE = [(SL - RP) - PL - (NL_f - (AG + SP)) + PG] - DT \quad . \quad (8)$$

Equation (8) directly defines the trade-off space of the independent factors for determining the ability of the system to detect $S(x, t, f)$. Signal excess "SE" is directly proportional to the performance of the system; as signal excess drops to zero, the ability of a system to detect and locate a source will also drop to zero. In other words, equation (8) is a primary model of the system performance (system performance equation).

The noise factor can be further parameterized as discussed in equation (2)

$$NL_f = [n_a(f) + n_a(t, f) + n_{ac}(t, f)] \quad (9)$$

where $n_{ac}(t, f)$ represents the components of the coherent clutter signals $s_k(x, t, f)$ that the signal processing operations $\Psi()$ were unable to mitigate. It may or may not be possible to estimate the individual components of NL_f prior to performing in situ measurements, but it is always possible to measure NL_f and come up with a statistical estimate of the combined noise.

In addition, propagation loss can be separated into geometric spreading GS , attenuation AN , and transmission factor TF losses

$$PL = GS + AN + TF \quad (10)$$

where geometrical spreading $GS = 20 \log r$ is spherical spreading for body waves and attenuation is described using the standard model $AN = 10 \log[\exp(2\pi r f / (Q_{p,s} c_{p,s}))]$ for compressional and shear waves separately. Transmission factor TF then captures simple scattering losses at interfaces and can be estimated using geometrical ray theory simple transmission coefficients. Transmission factor then is more appropriately parameterized as:

$$TF = \prod_{k=1}^N T_{k(i,j)}(p, c_{i,j}, \rho_{i,j}) \quad (11)$$

explained as the product of N transmission coefficients $T_{k(i,j)}$, where $T_{k(i,j)}$ is defined for the k^{th} discrete boundary between geologic layers i and j for N geologic boundaries lying between the source and receiver as a function of ray parameter p , and material densities ρ and P and S velocities c for layers i and j .

Observations and Analysis

Taking Equation (8) as the model for system performance, considering ($SL - RP$) together as the source level, and neglecting sensor sensitivity pattern SP , six main degrees of freedom are identified. The source level SL , propagation loss PL , and noise level NL_f are the three main uncontrolled factors all depending on the physical system prior to acquisition. The propagation loss PL , and noise level NL_f act directly to reduce and obscure the SOI. The factors of array gain AG , other processing gain PG , and the detection threshold DT represent the system components up to and including signal detection that can be controlled to affect the signal excess SE and register a detected signal.

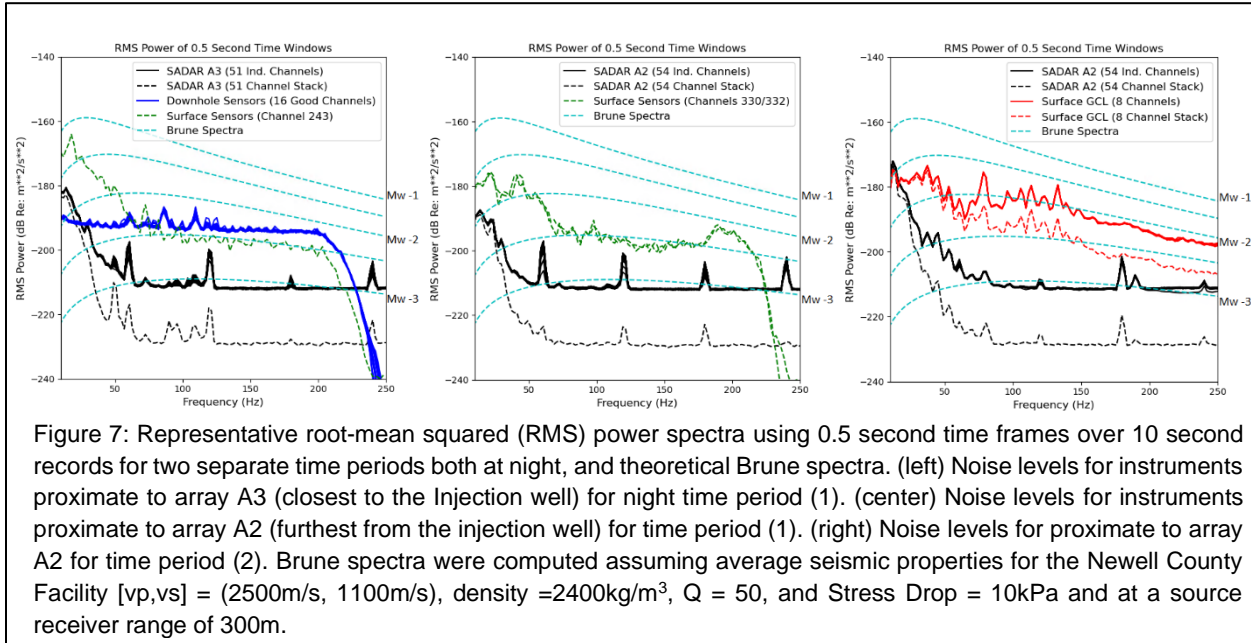
Examining the noise level NL_f , there are limited methods available for mitigating the combined noise terms. For sparse, single sensors in passive monitoring configurations, the most effective way to minimize recorded noise levels is to place sensors at depth to reduce the influence of surface noise. Although frequency band filters are always an option, there is no option for filtering based on wavenumber using single sensor emplacements. However, a phased array designed for a specific range of seismic wave frequencies and propagation speeds enables arbitrary directional beamforming, allowing the level of noise components that have uncorrelated frequency-phase-time relationships and randomized wavenumber attributes to be reduced via averaging across the array channels.

Figure 7 summarizes results comparing the noise levels of SADAR arrays against the other seismic instruments located at the site and shown in Figures 3 and 4. We focus on the noise levels recorded on the temporary surface GCL-3C geophone cluster (in red, Figure 7 right graph), the permanent 3C geophones emplaced at 1m depth and closest to the SADAR arrays (in green, Figure 7 left and center graph), and the downhole vertical array of 3C geophones (in blue, Figure 7 left graph), in comparison to arrays A3 and A2 which are emplaced closest and furthest from the injection well respectively. The surface sensors located near the SADAR arrays record elevated noise spectral levels compared to the SADAR arrays. Our experience at the NCF indicates this difference is typical for the variety of noise conditions at the site. The spectra for the downhole array shown in blue in Figure 7 right graph appear to have an elevated noise floor compared to the other systems. We expect that this is the result of non-optimal acquisition settings that have pushed the noise floor well above the ambient noise levels and as such we perform no further analysis on the downhole array for this work.

Neglecting the downhole array, all spectra indicate a region of ambient seismic noise between 0Hz and at least 70Hz where the levels fall off with frequency, transitioning to an approximate steady-state noise floor above 100Hz for the SADAR arrays and permanent phones (left and center graphs, Figure 7). The spectra for the surface-emplaced GCL cluster eventually transitions to approximate steady-state noise levels above ~400Hz (not shown). We expect that the approximate steady-state noise levels reflect the combination of sensor and acquisition system self-noise processes, which should have basically gaussian distributions.

The difference in noise levels for the single channel surface and near-surface sensors compared to the single channels of the SADAR arrays for the band 30Hz-100Hz is between ~15dB-25dB for the GCL sensors and A2 and averages ~19dB for the geophones at 1m depth. For frequencies greater than 100 Hz the difference in the noise levels on the GCL cluster single channels and the

A2 single channels ranges between ~8dB-16dB, and for the geophones at 1m depth the average is ~13dB. This reduction in the noise level between the single geophones and the individual sensors for the SADAR arrays is provided by increasing emplacement depth alone.



The channels in the SADAR arrays and the GCL cluster were then stacked to form the incoherent trace, and the spectra were determined as shown in Figure 7. The result of the incoherent summation for the SADAR arrays is an indication of array gain but does not include the gain due to the directional wavenumber filter that beamforming provides. The resulting spectra for the SADAR arrays, shown as the black dotted line in Figure 7 graphs for the SADAR arrays, indicate that steady state noise level above 100 Hz is suppressed by ~17 dB compared to the SADAR array single channels, which agrees with the theoretical $10 \cdot \log(N)$ figure (Urlick, 1983). The spectra of the incoherent summation for the GCL cluster, shown as and the red dotted line in Figure 7 right graph, indicates that at frequencies greater than ~90Hz, although the sensors were located within a distance that should preclude noise independence, there are some random components of the noise that are suppressed by ~6 dB which is less than what would be expected for uncorrelated noise.

Looking in the band 40Hz-100Hz, which is the main band for detecting microseismic events at the NCF, and comparing the gain against noise for the SADAR arrays using the incoherent sum vs. single channel measurement, for A2 the gain is 8-17dB and for A3 gain averages ~16dB. In this same band, Figure 7 (left and center) shows the difference in the noise spectra from the incoherent sum for the SADAR arrays compared to the near-surface geophones averages ~36dB for A2 and ~34dB for A3. These gain estimates over the single channel surface emplacements are then due to the combination of deploying the arrays at depth and the coherent processing array gain.

The spectral level in the frequencies below 30Hz is dominated by more coherent ambient seismic noise and clutter signals. This band is at least a factor of 3 below the lowest array design

frequency so we would not expect any significant noise suppression from an incoherent sum because at corresponding wavelengths the noise on the separate channels should not be independent. We infer that the gain over the single channel emplacements in this band is due to emplacement depth alone.

Examining the incoherent sum for the SADAR arrays plotted as the dotted black line in Figure 7, and in consideration of Equation (8), this line represents the summed effect of the noise level NL_f from all contributions and the array gain AG .

As stated in the mathematical performance equation (Equation (8)), the ambient and clutter noise factors limit ability of a passive seismic monitoring system to detect, locate, and measure microseismic events. Considering theoretical Brune (1970, 1971) spectra as shown in Figure 7 for five different sized microseismic events from Mw -3 up to Mw -1 at a source-receiver range of 300m, then even under ideal background noise levels the surface sensors would struggle to detect events smaller than Mw -2. However, using the optimal beamformed trace it should be possible for the network of SADAR arrays to detect Mw -2.5 events with enough signal excess SE to automatically detect the event, identify phase arrival times, and perform a location, for events occurring throughout the monitored volume.

Again examining Equation (8) for SE, the propagation loss PL factor acts against the source level SL . The terms that contribute to the propagation loss are functions of range as shown in Equation (10) and the following material. Detection performance versus range and PL then can be estimated from the bulletin of located events (Zhang *et al.*, 2022; Zhang *et al.*, 2023), using event size and the peak signal values measured from the optimal beam. The goal is to examine the measured received signal power for each array as a function of the event source level (i.e. magnitude) versus range for events with low location uncertainty, then graphed as a function of event-to-array range, as shown in Figure 8. Peak amplitude (particle velocity) is measured from the optimal beam of each array and converted to power in dB, and then plotted versus range, using color to indicate event magnitude value. Using 50 located high-confidence events of maximum ~20 m semi-major axis and maximum ~30 meters uncertainty in depth with good SNR, yields one measurement per array for a total of 200 measurements, but they cannot be considered as completely independent.

For purposes of showing magnitude-range detection characteristics, curves of theoretical signal power versus range for example events are plotted as dashed black lines overlaying the Figure 8 scatter plot assuming geometrical spreading is the only source of propagation loss. Also plotted are the measured average individual channel noise power levels for the SADAR arrays (red dashed line) and then the approximate values for noise levels taking into account the gain measured in the optimal beam for ~10 dB minimum gain to ~18 dB maximum expected gain (green dashed line and dot-dash line respectively).

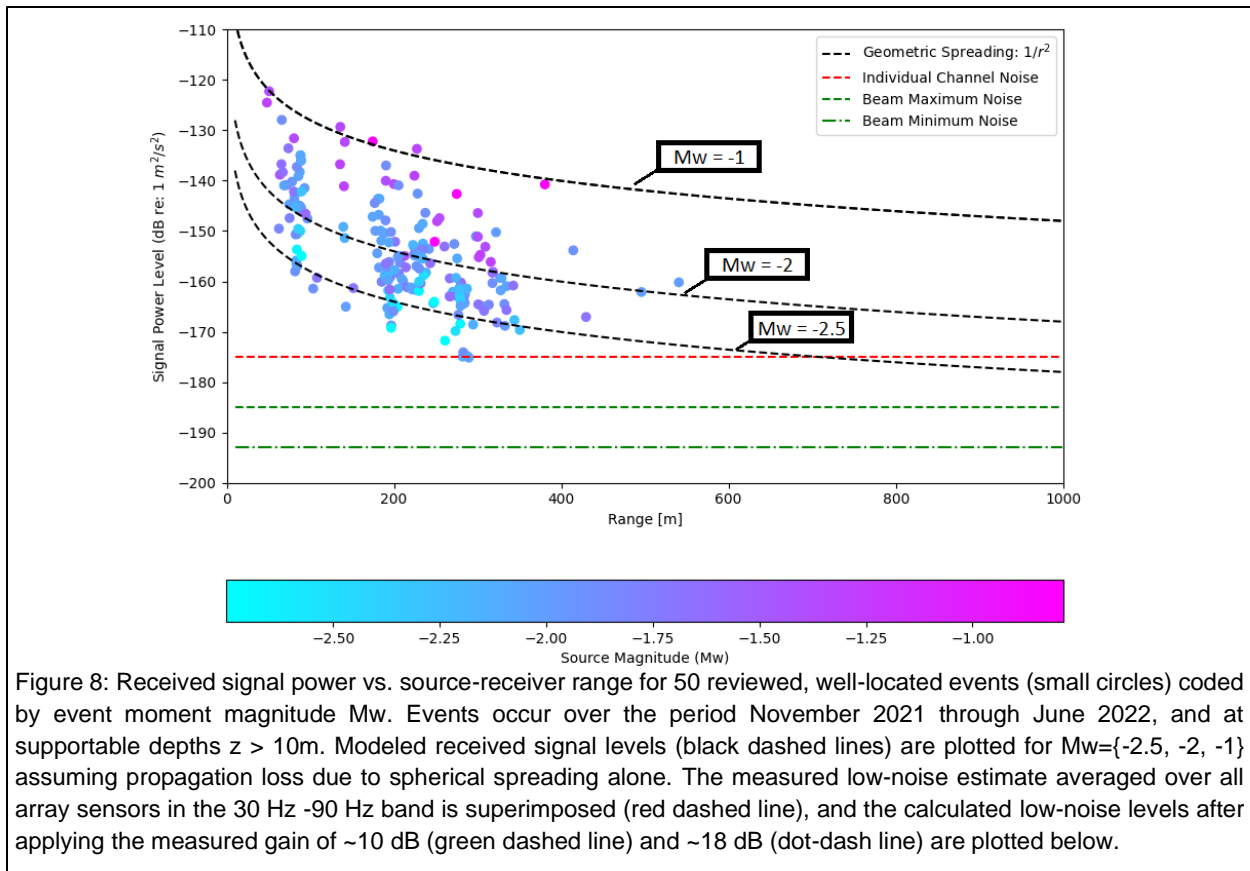


Figure 8: Received signal power vs. source-receiver range for 50 reviewed, well-located events (small circles) coded by event moment magnitude M_w . Events occur over the period November 2021 through June 2022, and at supportable depths $z > 10\text{m}$. Modeled received signal levels (black dashed lines) are plotted for $M_w = \{-2.5, -2, -1\}$ assuming propagation loss due to spherical spreading alone. The measured low-noise estimate averaged over all array sensors in the 30 Hz -90 Hz band is superimposed (red dashed line), and the calculated low-noise levels after applying the measured gain of $\sim 10\text{ dB}$ (green dashed line) and $\sim 18\text{ dB}$ (dot-dash line) are plotted below.

The integrated information in Figure 8 suggests that for events with magnitudes below $\sim M_w = -2.5$, reliable detection requiring a signal excess peak signal power of $SE \geq \sim 10\text{ dB}$ and a high confidence location of maximum $\sim 20\text{ m}$ semi-major axis and maximum of $\sim 30\text{ meters}$ uncertainty in depth, is limited to a maximum range between 600 and 800 meters. This in turn suggests that the M_w magnitude of completeness for the SADAR system bulletin of locatable microseismic events limited to the volume covered by the SADAR network should be no greater than $\sim M_w = -2.5$. However, the upper dashed green line in Figure 8 also suggests that the threshold for event detection at any individual SADAR array at source-receiver ranges out to 800m is substantially lower than $M_w = -2.5$, which agrees with the estimates of received signal levels using a Brune (1970, 1971) model plotted in Figure 7.

Conclusions and Outlook

A sparse network of four permanent SADAR compact volumetric phased arrays that Quantum Technology Sciences installed at the CaMI Newell County Facility has demonstrated a robust capability for passive monitoring of microseismic events over the past year. This year-long continuous seismic signal collection allows the assessment of several of the factors impacting phased array and network performance for microseismic event detection and location. After a brief discussion acknowledging the history of array development, we review several

considerations for the designs of arrays in general and phased arrays in particular. We presented a mathematical performance model based on the sonar equation framework to aid in understanding the factors contributing to the signal-to-noise ratio that limit detection, and therefore the ability of any system to locate and characterize microseismic events.

Measurements in the frequency domain indicate that coherent processing of the data acquired using SADAR phased arrays provides noise level suppression from 10dB to ~18dB over the individual array channels. The total measured noise suppression of beamformed SADAR arrays over the closest surface single stations is at least ~30dB, reflecting the combined effects of moderate emplacement depths and coherent processing. Graphing the received signal levels as a function of range and event source level (M_w magnitude) illustrates the range dependent propagation loss. Signal levels versus range in comparison with noise levels suggest that $M_w=2.5$ events form the lowest magnitude of completeness for the bulletin of events from the SADAR network. However, both the measured received signal versus range and the estimates of expected signal spectra using the Brune (1970, 1971) model suggest that the limiting threshold for event detection is substantially below that magnitude.

These measured performance examples combine factors from the presented performance model. Noise level NL_f and array gain AG are combined producing the low noise estimates shown in Figure 7; source level SL and propagation loss PL are combined to produce the received signal power estimates of Figure 8. An extension of this work then is to complete the analysis and produce estimates of the individual performance equation factors as well as breaking out the components of the noise level and propagation loss as represented in Equation (9) through Equation (11). The next goal using this model framework and ongoing measurements is estimating the lowest source levels of microseismic detection and likewise for location for the area within the SADAR network at the NCF as a function of depth layer to arrive at a complete performance assessment.

Acknowledgements

Quantum Technology Sciences, Inc., is a wholly owned subsidiary of Geospace Technologies Corporation, Inc. We acknowledge CMC for providing access to the CaMI Newell County Facility to enable installation of the SADAR system, and for sharing the data from the surface and downhole networks. The Newell County Facility is supported by funding from the Global Research Initiative at the University of Calgary from the Canada First Research Excellence Fund and from the CaMI Joint Industry Project. CMC is also acknowledged for providing operational data from the site.

References

- Aki, K., and P. G. Richards, 1980, Quantitative Seismology. Theory and Methods. Freeman, San Francisco.
- Abraham, D. A., 2019, Underwater Acoustic Signal Processing, Springer Nature Switzerland, Cham.
- Ainslie, M. A., 2010, Principles of Sonar Performance Modeling. Springer-Verlag Berlin.
- Ammon, C. J. A. A. Velasco, T. Lay, T. C. Wallace, 2021, Foundations of Modern Global Seismology. Elsevier, San Diego.

- Baeten, G., V. Belougne, T. Brice, L. Commbee, E. Kragh, A. Laake, J. Martin, J. Orban, A. Özbek, and P. Vermeer, 2001, Acquisition and processing of single sensor seismic data: ASEG Extended Abstracts, 2001:1, 1-4, DOI: 10.1071/ASEG2001ab011.
- Boatwright, J. and G. L. Choy, 1986, Teleseismic estimates of the energy radiated by shallow earthquakes. *Journal of Geophysical Research* 91, pp. 2095-2112.
- Boatwright, J., G. L. Choy, and L. C. Seekins, 2002, Regional estimates of radiated seismic energy. *Bulletin of the Seismological Society of America* 92, pp. 1241-1255.
- Brune, J. N., 1970, Tectonic stress and the spectra of seismic shear waves from earthquakes: *Journal of Geophysical Research*, 75, 4997-5009.
- Brune, J., 1971, Correction, *Journal of Geophysical Research*, 75, 5002.
- Burdic, W. S., 1991, *Underwater Acoustics System Analysis*, Second Edition, Prentice-Hall, Englewood Cliffs.
- Cary, W. M., 1998, The determination of signal coherence length based on signal coherence and gain measurements in deep and shallow water, *Journal of the Acoustical Society of America* 104, 831-837.
- Cordsen, A., M. Galbraith, and J. Peirce, 2000, *Planning Land 3-D Seismic Surveys*: Society of Exploration Geophysicists.
- Cortes, D. M., and J. Caldwell, 2015, Single geophone versus geophone array: a field study performed in Columbia: SEG Technical Program Expanded Abstracts: 1-5. <https://doi.org/10.1190/segam2015-5877389.1>.
- Choy, G. L., J. L. Boatwright, S. Kirby, 2001, The radiated seismic energy and apparent stress of interplate and intraplate earthquakes at subduction zone environments: implications for seismic hazard estimation. USGS Open File Report 01-0005, U.S. Geological Survey.
- Dean, T., J. C. Dupuis, and R. Hassan, 2015, The coherency of ambient seismic noise recorded during land surveys and the resulting implications for the effectiveness of geophone arrays. *Geophysics* 80, P1-P10.
- Denham, D., 1963, The uses of geophone groups to improve the signal to noise ratio of the first arrival in refraction shooting. *Geophysical Prospecting* 11, 389-408.
- Dongas, J. M., and D. C. Lawton, 2015, Development and characterization of a geostatic model for shallow CO₂ injection, CREWES research report 27, 1-34.
- Douglas, A., 2013, *Forensic seismology and nuclear test bans*: Cambridge University Press.
- Eaton, D. W., 2018, *Passive seismic monitoring of induced seismicity*: Cambridge University Press, New York, NY.
- English, J. M., and K. L. English, 2022, An overview of carbon capture and storage and its potential role in the energy transition: *First Break*, 40, 35-40
- Frank, J., and J. D. Richards, 2008, Phased array radar antennas, in M.I. Skolnik, ed., *Radar Handbook*, 3rd edition: McGraw Hill, 13.1-13.74.
- Global CCS Institute (GCCSI) Annual Report, 2021, Global Status of CCS- CCS accelerating to net zero, <https://www.globalccsinstitute.com/wp-content/uploads/2023/01/Global-Status-of-CCS-2021-Global-CCS-Institute-1121-1-1.pdf>, last access: January 11, 2023.
- Global CCS Institute (GCCSI) Annual Report, 2022, Global Status of CCS – Building momentum as we shift into a phase of action, <https://status22.globalccsinstitute.com/>, last access: January 11, 2023.

- Havskov, J. and G. Alguacil, 2006, *Instrumentation in Earthquake Seismology*. Springer, Dordrecht.
- Havskov, J. and L. Ottemoller, 2010, *Routine Data Processing in Earthquake Seismology*. Springer Science+Business Media, Dordrecht.
- Husebye, E.S., Ruud, B. O., 1989, Array seismology – past, present, and future developments, in *Observatory Seismology – A Centennial Symposium For The Berkeley Seismographic Stations*, Joe J. Litehiser ed., University of California Press.
- IEA, 2020, *CCUS in Clean Energy Transitions*, IEA, Paris <https://www.iea.org/reports/ccus-in-clean-energy-transitions> (accessed Dec. 10th, 2022)
- IEA, 2021, *Net Zero By 2050: A Roadmap for the Global Energy Sector*, IEA, Paris <https://www.iea.org/reports/net-zero-by-2050> (accessed Jan. 13th, 2023) .
- IPCC 2021. *Climate Change 2021: The Physical Science Basis. Contribution of Working Group I to the Sixth Assessment Report of the Intergovernmental Panel on Climate Change*. Cambridge University Press, UK.
- Jafari Raad, S.M., Lawton D.C., Maidment, G., and Hassanzadeh, H., 2021, Transient non-isothermal coupled wellbore-reservoir modeling of CO₂ injection - Application to CO₂ injection tests at the CaMI FRS site, Alberta, Canada: *International Journal of Greenhouse Gas Control*.
- Johnson, C. H., 1939, Steady state polar sensitivity curves. *Geophysics* 4, 33-52.
- Kao, H., and S.-J. Shan, 2004, The source-scanning algorithm: mapping the distribution of seismic sources in time and space: *Geophysical Journal International*, 157(2), 589-594.
- Klipsch, P. W., 1936, Some aspects of multiple recording in seismic prospecting, *Geophysics* 1, 365-377.
- Krohn, C., S. Ronen, J. Deere, and N. Gulunay, 2008, Introduction to this special section—Seismic Noise. *The Leading Edge* 27, 163-165.
- Lawton, D. C., J. Dongas, K. Osadetz, A. Saeedfar, and M. Macquet, 2019, Chapter 16: Development and analysis of a geostatic model for shallow CO₂ injection at the Field Research Station, Southern Alberta, Canada, in T. Davis, M. Landro, and M. Wilson, eds., *Geophysics and Geosequestration*: Cambridge University Press, 280-296. DOI 10.1017/9781316480724.017.
- Lawton, D., T. Hinter, B. Kolkman-Quinn, J. Monsegny, M. Bertram, G. Maidment, 2022, Sparse Optimum-offset, Seismic Surveys for Monitoring Gigatonne-scale CCS Projects; presented at the SEG workshop:- Toward Gigatonnes CO₂ Storage — Grand Geophysical Challenge; 26-30 June 2022, Stanford, CA.
- Lay, T., and T. C. Wallace, 1995, *Modern Global Seismology*. Academic Press, San Diego.
- Macquet, M., D. Lawton, K. Osadetz, G. Maidment, M. Bertram, K. Hall, B. Kolkman-Quinn, J. Monsegny Parra, F. Race, G. Savard, Y. Wang, 2022, Overview of Carbon Management Canada's pilot-scale CO₂ injection site for developing and testing monitoring technologies for carbon capture and storage, and methane detection: *Recorder Focus Article*, 47, No. 01, April 2022.
- Michel, U., 2006, History of Acoustic Beamforming: in *Proceedings of the 1st Berlin Beamforming Conference*, 22-23 November, 2006.
- Mueller, T. J., editor (2002) *Aeroacoustic Measurements*, Springer-Verlag, Heidelberg.
- Muravieva, S., K. Osadetz, and D. C. Lawton, 2017, Petrographic assessment of the Upper Cretaceous Foremost Formation prior to CO₂ injection at Field Research Station, Newell County, Alberta; in *Perdersen, K., B. Kuntz, K. Latos,*

A. Fraser, R. Geuder, and J. Barclay, (eds.) Canadian Society of Petroleum Geologists, 2017 Core Abstract Booklet, Calgary, May 18-19, 2017, p. 27-31.

Newman, P., and J. T. Mahoney, 1973, Patterns - with a pinch of salt. *Geophysical Prospecting* 21, 197-219.

Nyffenegger, P. A., M. A. Tinker, J. Zhang, E. B. Grant, K. D. Hutchenson, and D. C. Lawton, 2022, Compact phased arrays for microseismic monitoring: *First Break* 40, 4, 69-74.

Osadetz, K. G., Lawton, D. C., Larter, S., Mayer, B., and Pederson, P. K., 2015, CMC Research Institutes' Countess well (10-22-17-16W4): the Upper Cretaceous succession at a unique subsurface laboratory and technology demonstration site: *GeoConvention, Conference Abstracts*.

Priestley, M. B. (1981). *Spectral Analysis and Time Series*. Academic Press.

Rassenfoss, S., 2023, Irregular is what's regular for CO2 storage plumes: *Journal of Petroleum Technology*, <https://jpt.spe.org/irregular-is-whats-regular-for-co2-storage-plumes>

Rieber, F., 1936, A new reflection system with controlled directional sensitivity, *Geophysics* 1, 97-106.

Ringrose, P., J. Andrews, P. Zweigel, A.-K. Furre, B. Hern, B. Nazarian, 2022, Why CCS is not like reverse gas engineering: *First Break* 40, 10, 85-91.

Rost, S., and C. Thomas (2002) Array seismology: methods and applications: *Reviews of Geophysics*, 20, 2-1 – 2-27.

Roux, P. F., J. Kostadinovic, J. Kostadinovic, T. Bardainne, E. Rebel, M. Chmiel, M. Van Parys, R. Macault and L. Pignot, 2014, Increasing the accuracy of microseismic monitoring using surface patch arrays and a novel processing approach, *First Break* 32, 95-101.

Savard, G., H. Gilbert, M. Macquet, D. Lawton, and J. Gu, 2020, Microseismic monitoring at a shallow injection site, the CaMI Field Research Station in Newell County, AB: *Geoconvention 2020 Virtual Event Conference Proceedings*.

Schweitzer, J., J. Fyen, S. Mykkeltveit, S. J. Gibbons, M. Pirli, D. Kühn, T. Kværna. (2012): Seismic Arrays. In: Bormann, P. (Ed.), *New Manual of Seismological Observatory Practice 2 (NMSOP-2)*, Potsdam : Deutsches GeoForschungsZentrum GFZ, 1-80. https://doi.org/10.2312/GFZ.NMSOP-2_ch9

Shapiro, S. A., and R. Schwarz, 1995, The effect of 3-D random inhomogeneities on kinematics of seismic waves, *SEG Technical Program Expanded Abstracts* : 1313-1316.

Shapiro, S. A., R. Schwarz, and N. Gold, 1996, The effect of random isotropic inhomogeneities on the phase velocity of seismic waves. *Geophysical Journal International* 127, 783-794.

Skolnik, M. I. (2001) *Introduction to Radar Systems*, third edition, McGraw-Hill, New York.

Smith, M. K., 1956, Noise analysis and multiple seismometer theory, *Geophysics* 21, 337-360.

Strobbia, C., T. Dean, S. Re, E. Ceragioli, D. Sweeney, and M. Nightingale, 2014, Fundamental noise—the key to recovering your signal: and integrated workflow for seismic survey design, *First Break* 40, 87-95.

Swanson, D. C., and R. L. Culver, 2017, Small-aperture array processing for passive multi-target angle of arrival estimation: *Journal Acoustical Society of Am.* 142, 2030-204, DOI: 10.1121/1.5006910.

Tinker, M, K. Hutchenson, P. Nyffenegger, K. Englehardt, and R. Lowther, 2021, Networked System and method for passive monitoring, locating or characterizing activities: U.S. Patent Application No. 17/480059, publication number US 2022/0091289, March 24, 2022.

Urlick, Robert J., 1983, *Principles of Underwater Sound*, 3rd Edition, Peninsula Publishing, Westport.

GeoConvention 2023

Van Trees, H. L., 2002, Optimum Array Processing: Wiley Interscience.

Vocke, C. P., Clarkson, C. R., Aquino, S., Vahedian, A., Lawton, D. C., Osadetz, K., and Ghanizadeh, A., 2016, Application of profile (probe) permeability and mechanical (rebound) hardness tests for characterization of fluid transport and geomechanical properties of selected formations in western Canada: GeoConvention 2016, Canadian Society of Petroleum Geologists, conference proceedings and online, 2016 May, extended abstracts.

Yang, T. C. 2006, Measurements of temporal coherence of sound transmissions through shallow water, Journal of the Acoustical Society of America 120, 2595-2614

Zhang, J., E. B. Grant, P. A. Nyffenegger, M. A. Tinker, K. D. Hutchenson, and D. C. Lawton, 2022, Seismic monitoring using compact phased arrays: CO2 sequestration monitoring: Second International Meeting for Applied Geoscience & Energy. August 2022, 483-487.

Zhang, J., K. D. Hutchenson, P. A. Nyffenegger, E. B. Grant, J. Jennings, M. Tinker, M. Macquet, D.C. Lawton, 2023, Performance comparison of compact phased arrays and traditional seismic networks for microseismic monitoring at a CO2 sequestration test site, The Leading Edge in press.

Ziomek, L. J. 1995, Fundamentals of Acoustic Field Theory and Space-Time Signal Processing: CRC Press.